High-Definition Mapping of Four Spatially Distinct Neutralizing Epitope Clusters on RiVax, a Candidate Ricin Toxin Subunit Vaccine

Ronald T. Toth IV,[a] Siva Krishna Angalakurthi,[a] Greta Van Slyke,[b]
David J. Vance,[b] John M. Hickey,[a] Sangeeta B. Joshi,[a] C. Russell Middaugh,[a]
David B. Volkin,[a] David D. Weis,[c] Nicholas J. Mantis[b]

Department of Pharmaceutical Chemistry and Macromolecule and Vaccine Stabilization Center, University of Kansas, Lawrence, Kansas, USA[a]; Division of Infectious Diseases, Wadsworth Center, New York State Department of Health, Albany, New York, USA[b]; Department of Chemistry and Ralph Adams Institute for Bioanalytical Chemistry, University of Kansas, Lawrence, Kansas, USA[c]

ABSTRACT RiVax is a promising recombinant ricin toxin A subunit (RTA) vaccine antigen that has been shown to be safe and immunogenic in humans and effective at protecting rhesus macaques against lethal-dose aerosolized toxin exposure. We previously used a panel of RTA-specific monoclonal antibodies (MAbs) to demonstrate, by competition enzyme-linked immunosorbent assay (ELISA), that RiVax elicits similar serum antibody profiles in humans and macaques. However, the MAb binding sites on RiVax have yet to be defined. In this study, we employed hydrogen exchange-mass spectrometry (HX-MS) to localize the epitopes on RiVax recognized by nine toxin-neutralizing MAbs and one nonneutralizing MAb. Based on strong protection from hydrogen exchange, the nine MAbs grouped into four spatially distinct epitope clusters (namely, clusters I to IV). Cluster I MAbs protected RiVax's α-helix B (residues 94 to 107), a protruding immunodominant secondary structure element known to be a target of potent toxin-neutralizing antibodies. Cluster II consisted of two subclusters located on the "back side" (relative to the active site pocket) of RiVax. One subcluster involved α-helix A (residues 14 to 24) and α-helices F-G (residues 184 to 207); the other encompassed β-strand d (residues 62 to 69) and parts of α-helices D-E (154 to 164) and the intervening loop. Cluster III involved α-helices C and G on the front side of RiVax, while cluster IV formed a sash from the front to back of RiVax, spanning strands b, c, and d (residues 35 to 59). Having a high-resolution B cell epitope map of RiVax will enable the development and optimization of competitive serum profiling assays to examine vaccine-induced antibody responses across species.

KEYWORDS antibody, biodefense, epitope, mass spectrometry, toxin, vaccine

Ricin is one of a small group of plant and bacterial toxins that are classified at the domestic and international levels as potential agents of bioterrorism (1, 2). Ricin is a product of castor beans (*Ricinus communis*), which are cultivated globally for their oils that are used in industrial lubricants, cosmetics, and biofuels. The toxin itself is an ~65-kDa glycoprotein that makes up ~5% of the dry weight of a castor bean. The toxin can be purified by relatively simple affinity chromatography (3, 4). On a cellular level, ricin exerts its cytotoxic effects through ribosome inactivation and triggering of programmed cell death (5). Ricin's binding subunit, ricin toxin B subunit (RTB), is a galactose/N-acetyl galactosamine (Gal/GalNAc)-specific lectin that promotes toxin entry into mammalian cells, while ricin's enzymatic subunit, RTA, is an RNA N-glycosidase (EC 3.2.2.22) that, when successfully delivered into the cytoplasm, cleaves the sarcin-ricin

loop (SRL) of 28S rRNA, thereby stalling ribosome translocation (6, 7). At the tissue level, particularly in the context of the lung, ricin induces severe inflammation with a marked influx of neutrophils, alveolar edema, and hemorrhages (8, 9). Nonhuman primates (rhesus macaques) exposed to ricin by aerosol succumb to the effects of the toxin within 24 to 52 h (8, 10). At this time, medical intervention following ricin exposure is strictly supportive (11).

Current efforts to develop a ricin toxin vaccine for military and other at-risk personnel are focused on two different recombinant RTA-based subunit antigens, RiVax and RVEc (12). RTA itself is a globular protein with a total of 10 β-strands (namely, strands a to j) and seven α-helices (namely, α-helices A to G). The toxin subunit folds into three distinct domains. Domain 1 (residues 1 to 117) is dominated by a six-stranded β-sheet, domain 2 (residues 118 to 210) is dominated by five α-helices, and domain 3 (residues 211 to 267) interfaces with RTB through hydrophobic interactions and a single disulfide bond (13, 14). RTA's active site constitutes a shallow pocket formed at the interface of the three domains (14, 15). Active site residues include Tyr80, Tyr123, Glu177, Arg180, and Trp211. RiVax is a full-length (267-amino-acid) variant of RTA with two point mutations, one (Tyr80Ala) that virtually abolishes RTA's RNA N-glycosidase activity and one (Val76Met) that disrupts a motif associated with vascular leak syndrome (VLS) (16, 17). The tertiary structure of RiVax is essentially identical to that of RTA, as demonstrated by X-ray crystallography (18). RVEc, by contrast, is a truncated version of RTA that lacks domain 3 (residues 199 to 267) and also a small hydrophobic loop in the N terminus (residues 34 to 43) (19–21).

Because human efficacy trials are not ethical in the case of biothreat agents, including ricin, the advanced development of vaccines and eventual marketing approval by the Food and Drug Administration (FDA) in the United States must adhere to the so-called Animal Rule, which states that a product will be approved only if there are well-defined correlates of protection in one or more animal models that are predictive of a response in humans (22). In the case of ricin toxin, neither serum antibody (Ab) titers nor toxin-neutralizing activities are likely to be sufficiently predictive of protective immunity across species to serve as stand-alone markers in vaccine evaluation studies (12, 23–25). However, we recently demonstrated that nonhuman primates and human volunteers vaccinated with RiVax had similar serum antibody profiles in a competition enzyme-linked immunosorbent assay (ELISA) performed with a limited panel of RTA-specific mouse IgG monoclonal antibodies (MAbs), including several with potent toxin-neutralizing activity (TNA) (10). In that study, the vaccinated nonhuman primates were protected against lethal-dose ricin challenge administered by aerosol. Immunity was attributed to the presence of vaccine-induced, ricin-specific IgG antibodies in serum and/or bronchial fluids.

We have previously argued that it is critical to define the antibody repertoire and B cell epitopes associated with protective immunity to ricin toxin for vaccine development (12). Characterization of different collections of RTA-specific MAbs has indicated that the antibody response to ricin toxin is dominated by nonneutralizing (and even some toxin-enhancing) antibodies (26–32). Neutralizing antibodies are relatively rare, estimated at ~10% of the total ricin-specific pool. Complicating matters is the fact that there is often a disconnect between *in vitro* toxin-neutralizing activity and the capacity of a given MAb to neutralize ricin in an animal model (28, 33). In other words, MAbs that have potent toxin-neutralizing activity in a cell-based assay may or may not passively protect mice from ricin intoxication. The two primary factors currently associated with *in vivo* toxin-neutralizing activity are relative binding avidity and epitope specificity (12, 18, 28, 30, 34, 35). B cell epitope mapping studies of RTA have been conducted using peptide arrays (pepscan), peptide affinity enrichment by phage display, site-directed mutagenesis, differential reactivity with *Ricinus communis* agglutinin 1 (RCA-1), competition ELISAs, and surface plasmon resonance (SPR) analysis (28, 30, 34, 36–38). X-ray crystallography is also being used to define the structural B cell epitopes on RTA, although these studies have been restricted (with one exception) to the use of single-domain camelid antibodies (37, 39–42).

TABLE 1 RTA-specific mouse MAbs used in this study

MAb	Subclass	Cluster	Reference
PB10	IgG2b	I	30
R70	IgG1		38
WECB2	IgG1		34
SyH7	IgG1	II	30
PA1	IgG1		34
TB12	IgG1		34
PH12	IgG1		34
IB2	IgG1	III	34
GD12	IgG1	IV	43
(JD4)[a]	IgG1		34

[a]MAb JD4 is indicated in parentheses to denote that it is a nonneutralizing antibody.

Extensive characterization and epitope mapping studies of our collection of toxin-neutralizing and nonneutralizing murine MAbs have suggested that there are at least four spatially distinct epitope clusters (namely, clusters I to IV) on RTA (Table 1) (30, 34). Cluster I is defined by three MAbs, namely, PB10, R70 (UNIVAX 70), and WECB2. All three MAbs have potent toxin-neutralizing activity and have been shown to passively protect mice against lethal-dose ricin challenge. Cluster II is defined by four MAbs (SyH7, PA1, TB12, and PH12), while clusters III and IV are defined by MAbs IB2 and GD12, respectively. The six MAbs from clusters II to IV neutralize ricin toxin *in vitro* and *in vivo* with roughly similar potencies (30, 34, 43). We tentatively assigned the locations of clusters I and II on the surface of RiVax based on strong reactivity of PB10 and R70 with peptides spanning residues 97 to 108 (corresponding to RTA's α-helix B) and on weak reactivity of SyH7 with peptides spanning residues 187 to 198 (corresponding to RTA's α-helix F) (30, 34, 44). The other MAbs (except for GD12, as noted below) were assigned to a cluster based on competitive binding assays, because they were not reactive with RTA peptide arrays.

The goal of the current study was to define at high resolution the epitopes on RiVax recognized by the nine toxin-neutralizing MAbs, as well as one nonneutralizing MAb (JD4), currently grouped within epitope clusters I to IV. Hydrogen exchange-mass spectrometry (HX-MS) was the method of choice based on recent success in a wide variety of pathogens, including HIV, the malaria parasite, *Neisseria meningitidis*, and *Staphylococcus aureus* (45–50). In a recent study, we successfully adapted HX-MS for the purpose of identifying epitopes recognized by a family of RTA-specific single-domain alpaca-derived antibodies (V_HHs) (51). We also used HX-MS to assist in epitope refinement of a subset of the 68 V_HHs described in a companion paper (71). We now report the contact points on RiVax recognized by 10 MAbs in epitope clusters I to IV. The results afforded by HX-MS validate, for the most part, the previous competition ELISAs and epitope mapping studies. More importantly, they provide a rationale to begin the development of much-needed preclinical assays to gauge the integrity of toxin-neutralizing epitopes on the vaccine antigen and in the development of sensitive competitive binding assays for serum profiling to examine vaccine-induced antibody responses across species.

RESULTS

Four distinct clusters of neutralizing B cell epitopes on RiVax. We have previously assigned a collection of nine RTA-specific, toxin-neutralizing MAbs into four competition clusters (clusters I to IV), based on the results of pepscan analysis, reactivity with RTA point and deletion mutants, and competition ELISAs (Table 1; see also Table S1 and Fig. S1 in the supplemental material) (30, 34, 43, 44). PB10, R70, and WECB2 were assigned to cluster I, while SyH7, PA1, TB12, and PH12 constitute cluster II (Table 1; see also Fig. S1). Cluster III is defined by IB2, while cluster IV has been defined historically by GD12 (34). However, the competition matrix in Fig. S1 indicates that GD12 partially competes with PB10 and R70, suggesting that clusters I and IV may be adjacent to each
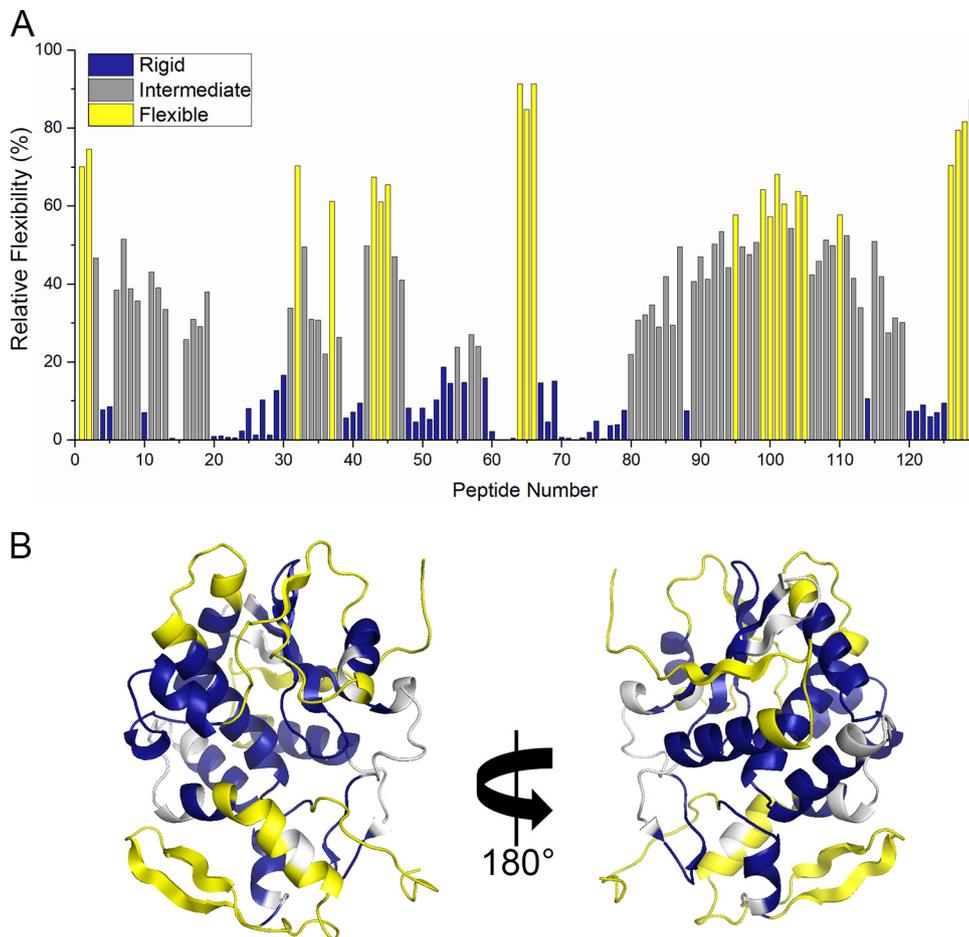
FIG 1 Relative levels of backbone flexibility of RiVax, as determined by HX-MS. RiVax was subjected to HX-MS analysis, as described in Materials and Methods. The extent of hydrogen exchange (HX) at 13 s for each RiVax peptide is shown in panel A. The peptides are color coded according to the results of *k*-means categorization as follows: rigid, blue; intermediate, gray; flexible, yellow. The peptide number indicates a sequential arrangement from the N terminus to the C terminus. The peptide assignments are provided in Table S1 in the supplemental material. (B) The flexibility categories mapped onto the structure of RiVax.

other. A tenth nonneutralizing MAb, JD4, was grouped within cluster IV based on its competition with GD12 (see Table S1 and Fig. S1).

RiVax's regions of intrinsic flexibility and rigidity. HX-MS is increasingly being used for the purpose of B cell epitope identification (47, 49, 50, 52, 53). The general principles of HX-MS and how the technique relates to other epitope mapping strategies have been covered in several recent reviews (45, 54). In a particularly informative study, Malito and colleagues subjected a single MAb directed against factor H binding protein from *Neisseria meningitidis* to epitope mapping by peptide array, HX-MS, and X-ray crystallography (50). Although HX-MS lacks the atomic resolution of X-ray crystallography, the two techniques were in congruence in terms of defining the primary MAb contact regions on the target antigen.

With the goal of using HX-MS for epitope mapping purposes in the case of ricin, we first established the baseline backbone flexibility of RiVax to enable us to properly evaluate changes in protection upon antibody binding. RiVax was subjected to HX and quenched after 13 s of labeling before being subjected to pepsin digestion and MS analysis, as described in Materials and Methods. The distribution of backbone flexibility values was best described by categorization into three groups, according to *k*-means clustering: rigid, intermediate, and flexible. There were clearly defined regions of flexibility and rigidity across the different RiVax secondary structural elements (Fig. 1).

Here, and in subsequent figures, the peptides are numbered sequentially from the most N-terminal peptide to the most C-terminal peptide (see Table S2 in the supplemental material). For a point of reference, flexible regions include the N and C termini, the proximal end of α-helix A, the proximal end of α-helix B, β-strand a, β-strand h and surrounding loops, the loop connecting α-helices D, E, and G, and the β-sheet formed by β-strands i and j (Fig. 1; yellow). Rigid regions include portions of α-helix A, the small β-sheet formed by strands b and c, β-strands d, e, f, and g and connecting loops, the C-terminal half of α-helix B, α-helices C and D and the connecting loop, α-helices E and F and the connecting loop, the N-terminal portion of α-helix G, and the 3/10 helix in the C-terminal region (Fig. 1; blue). The remaining secondary structural elements were classified as intermediate.

HX-MS analysis of RiVax bound to cluster I MAbs (PB10, R70, and WECB2). To apply HX-MS for epitope mapping of RiVax, we initiated studies with PB10, the murine MAb that defines cluster I (30). PB10's epitope has been assigned with confidence to a linear stretch of residues within RiVax's α-helix B (residues 98 to 106), as demonstrated by pepscan analysis and affinity enrichment studies performed with a phage-displayed peptide library (30, 44). These studies are supported by additional epitope mapping experiments using a collection of RTA site-directed point and deletion mutants (34).

HX-MS analysis of RiVax was performed at five exchange times between 13 s and 24 h, using protocols essentially in line with well-established HX-MS methodologies (Fig. 2) (55–58). For the labeling studies, PB10 was at 2-fold molar excess relative to RiVax to favor complex formation. As expected, there were distinct differences in the rates of HX by peptides in the presence of PB10. As shown in Fig. 2A and B, the rate of HX by peptide 1 (residues 0 to 11) was unaffected by PB10, while HX of peptide 38 (residues 93 to 107) was considerably slower in the presence of PB10. A reduction in HX across a peptide is interpreted as protection due to protein-protein contacts and, therefore, diagnostic of epitopic regions (45). The magnitude of this protection was quantified using the deuteration difference normalized by maximal deuteration as follows:

$$\Delta \mathrm{HX} = \frac{\Delta m_{\mathrm{bound}} - \Delta m_{\mathrm{free}}}{\Delta m_{\infty}}$$

where Δm denotes the measured mass increase for each peptide and the infinity subscript indicates HX measured in a deuteration control. The ΔHX data from each of the five HX times are shown in Fig. 2C to G. These values were then averaged ($\Delta\overline{\mathrm{HX}}$) as shown in Fig. 3, using a methodology described elsewhere (R. Toth IV, S. K. Angalakurthi, M. J. Rudolph, D. Volkin, C. R. Middaugh, N. J. Mantis, and D. Weis, unpublished data), and were applied successfully to V_HH-RTA interactions, where we compared the HX-MS output to a known X-ray crystal structure (51). The magnitudes of altered HX were classified by k-means clustering into four categories and were color coded accordingly as follows: strong protection, deep blue; intermediate protection, light blue; no protection, gray; deprotection, yellow. Averaged or summed HX differences are used widely in the HX-MS field, as noted in the citation provided above. It has been shown, for example, that the area between HX curves is proportional to the change in protection from HX (56, 58). Specifically, for HX measurements that are equally spaced on a log scale, the area between the HX curves is proportional to the average HX difference that we have used, i.e., $\Delta\overline{\mathrm{HX}}$. Therefore, this form of representation is used throughout the remainder of this work.

To visually define the locations of altered HX, the averaged differences were mapped onto the surface of RiVax (Fig. 4A). In the presence of PB10, HX-MS revealed strong protection (i.e., slower hydrogen exchange) across peptides 34 to 36 and peptides 38 to 41, corresponding to RiVax residues 94 to 107 (Table 2 and Fig. 2), which is consistent with PB10's proposed core epitope based on peptide mapping studies (30, 44). Peptide 114, which encompasses RiVax residues 243 to 244 and includes the loop following strand j, was also strongly protected, although its distance from PB10's core binding site would suggest that its protection is due to allostery rather than direct contact (Fig. 4A). PB10 induced intermediate degrees of protection at two different
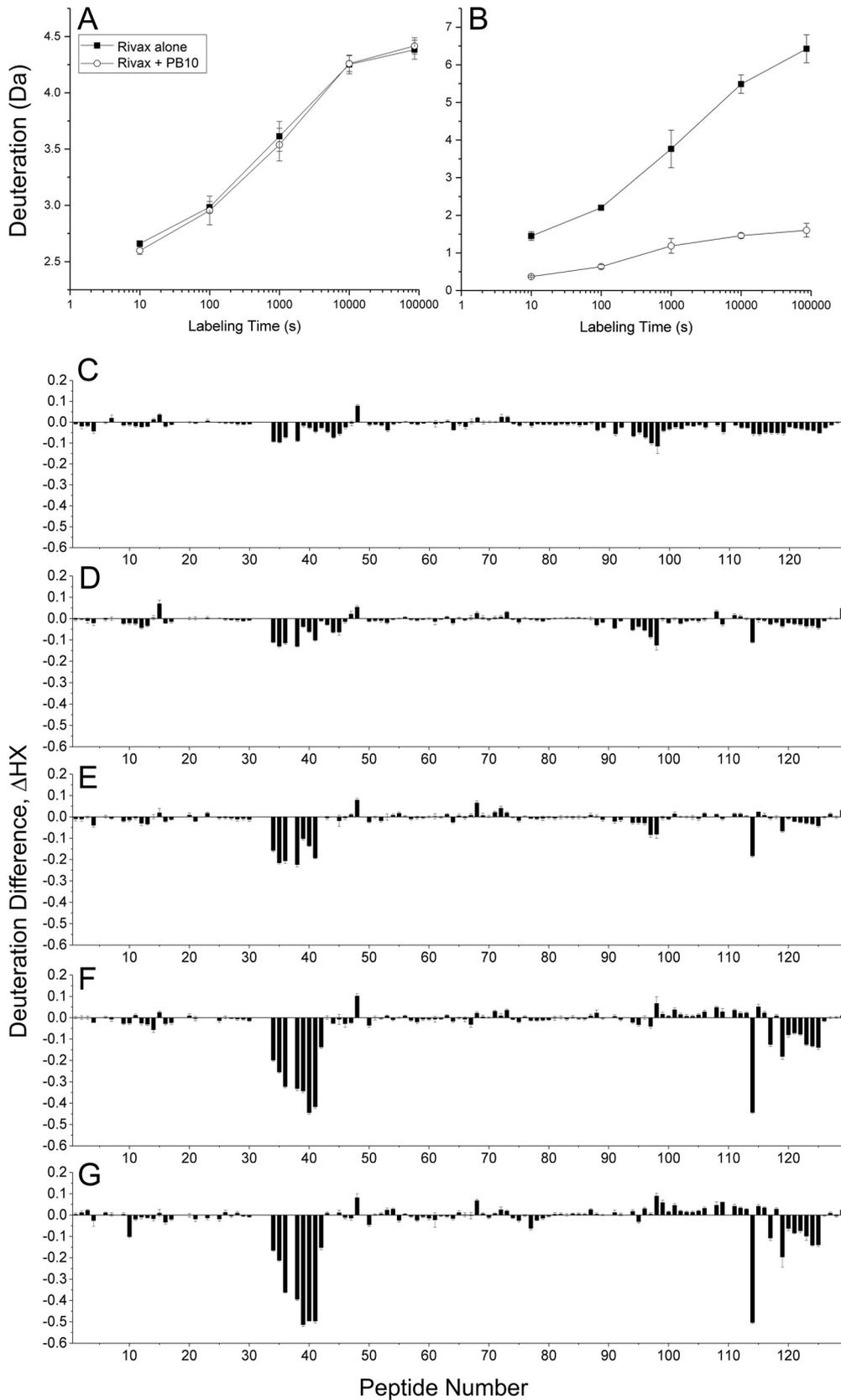
FIG 2 HX-MS analysis of RiVax in the presence of PB10. RiVax was subjected to HX-MS analysis in the absence or presence of MAb PB10. (A and B) HX kinetics of two representative RiVax peptides. Panel A shows peptide 1 (residues 0 to 11), where the rate of HX was unaffected by PB10. Panel B shows peptide 38 (residues 93 to 107), where the rate
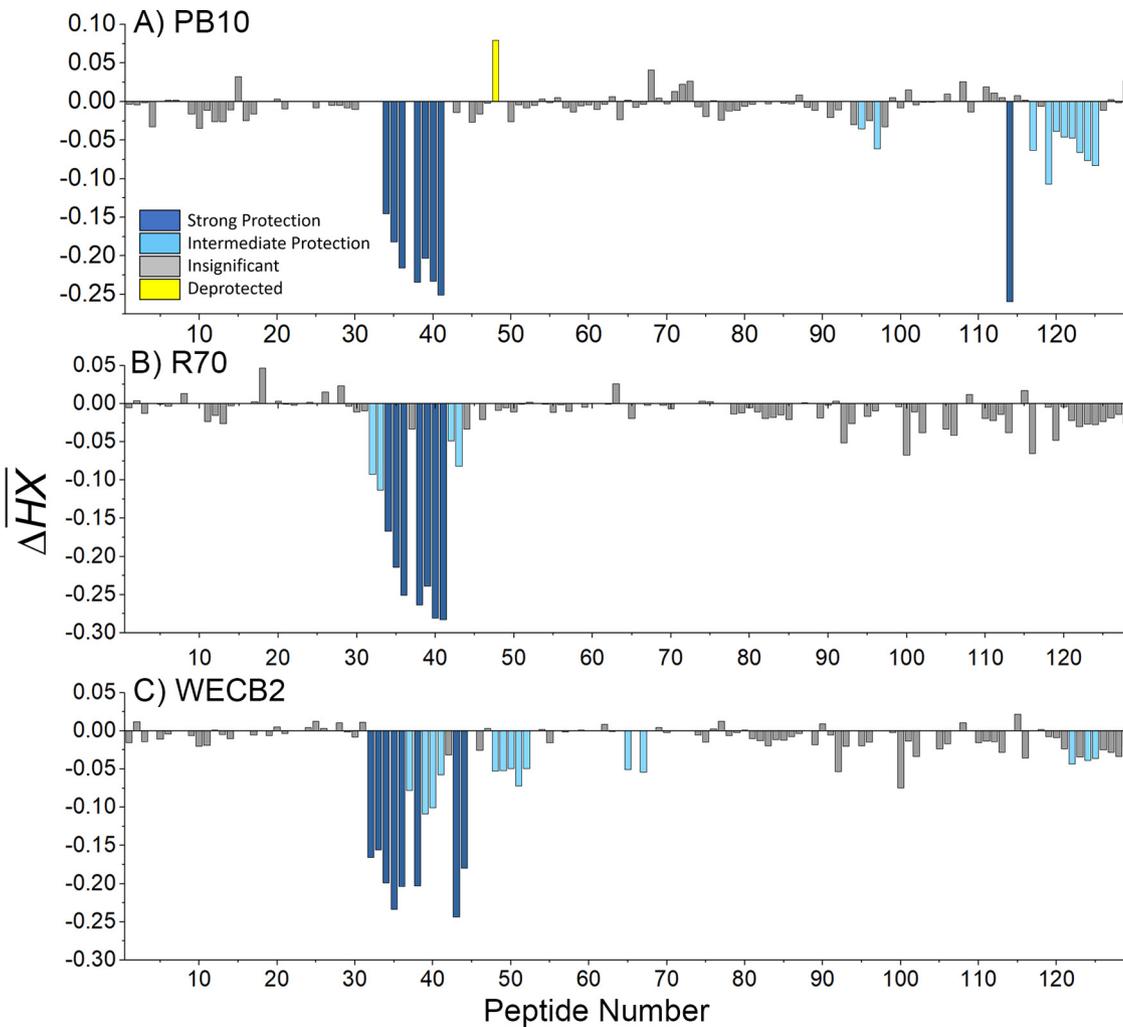
(Continued on next page)

FIG 3 Relative levels of protection of RiVax peptides by PB10, R70, and WECB2, as defined by HX-MS. RiVax was subjected to HX-MS analysis in the presence of (A) PB10, (B) R70, and (C) WECB2. The $\Delta\overline{HX}$ values for each RiVax peptide are shown and colored according to their k-means categorization as follows: strong protection, deep blue; intermediate protection, light blue; insignificant protection, gray; deprotection, yellow.

sites, i.e., residues 209 to 218 (represented by peptides 95 and 98) and residues 244 to 256 (peptides 117 and 119 to 125) near RiVax's C terminus. Discerning whether the observed intermediate regions of protection constitute actual antibody binding sites, as opposed to distal effects, is difficult and we have chosen in this study to limit our conclusions to areas of strong protection. PB10 illustrates the challenges associated with interpreting intermediate protection. Residues 244 to 256 are situated on the face opposite α-helix B and are therefore not readily accessible to PB10 when bound to its core epitope, as defined by strong protection across two or more adjacent peptides. Residues 209 to 218 (encompassing α-helix G) could conceivably constitute a contact point based on its spatial location, but competition assays suggest otherwise (as noted below). Finally, we noted that RiVax peptide 48 (residues 125 to 129; α-helix C) was deprotected (i.e., showed faster hydrogen exchange) in the presence of PB10 (Fig. 3A

FIG 2 Legend (Continued)
of HX was substantially slowed by PB10. The filled squares denote RiVax alone. The open symbols denote RiVax bound to PB10. (C to G) The uptake at each HX time for RiVax labeled alone was subtracted from the uptake in the presence of PB10, resulting in mass differences that are plotted at (C) 13 s, (D) 100 s, (E) 1,000 s, (F) 10,000 s, and (G) 86,000 s (24 h) of labeling. Error bars represent the standard deviations of triplicate measurements propagated through the mass differences.
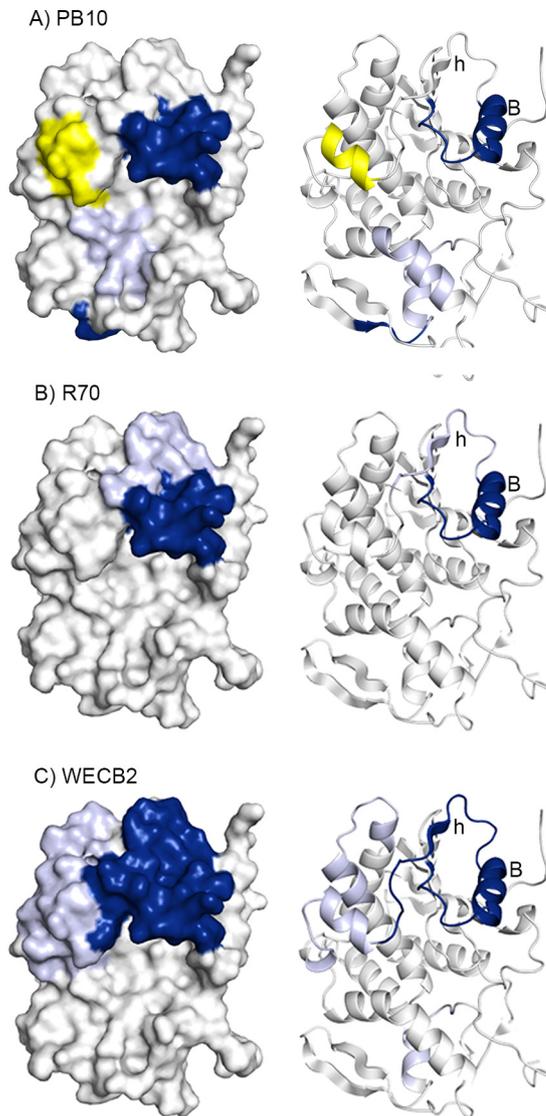
FIG 4 Visual presentation of the core epitopes of PB10, R70, and WECB2 on RiVax. HX protection categories, as defined in the Fig. 3 legend, are shown mapped onto the structure of RiVax for (A) PB10, (B) R70, and (C) WECB2. The image is color coded according to the Fig. 3 legend. The most relevant secondary structures, β-strand h and α-helix B, are labeled.

and 4A). Deprotection near α-helix C indicates that the backbone amine residues are more susceptible to hydrogen exchange in the presence of PB10, most likely due to allosteric effects as a consequence of antibody contact with α-helix B. It is interesting that peptide 14 (residues 125 to 129) was classified as being rigid (Fig. 1) and therefore not particularly prone to HX at baseline. Thus, even small allosteric changes in back-bone flexibility would result in notable deprotection.

We next investigated the two other cluster I MAbs, R70 and WECB2. On the basis of peptide reactivity, binding to RTA deletion and point mutants, and competition with PB10, it is proposed that R70 recognizes a linear epitope encompassing portions of α-helix B (residues 97 to 108), whereas WECB2 binds a conformational epitope including α-helix B (34, 38, 44). The results of HX-MS epitope mapping of R70 and WECB2 are summarized in Table 2 and Fig. 3 and 4. We observed strong protection for R70 across the entirety of α-helix B (residues 94 to 107; peptides 34 to 41). In this respect, R70 is identical to PB10. In the case of R70, however, there were additional sites of interme-diate protection in peptides bracketing α-helix B which could have been due to

TABLE 2 Summary of HDX analysis of RiVax bound by cluster I to IV MAbs

| MAb | Cluster | Strongly protected elements of RiVax[a] | | |
		Peptide no.	Residue no.	Secondary structure(s)
PB10	I	34–36, 38–41 114	94–107 243–244	α-Helix B
R70		34–41	94–107	α-Helix B
WECB2		32–36 38 43–44	94–107 95–107 110–122	α-Helix B α-Helix B β-Strand h
SyH7	II	2–4 80–86	14–24 184–207	α-Helix A α-Helix F, α-helix G
PA1		80–85	184–204	α-Helix F, α-helix G
TB12		16–18 66	60–69 155–164	β-Strand d α-Helices D-E
PH12		17–19 65–66	62–69 154–164	β-Strand d α-Helices D-E
IB2	III	46–50 52 88, 89, 91 123–124	121–135 129–135 207–217 251–254	α-Helix C α-Helix C α-Helix G
GD12	IV	8, 9, 11–13	35–59	β-Strands b, c, and d
JD4		123–125	251–255	

[a]Peptides and corresponding residues on RiVax are indicated in Table S1.

additional antibody contacts (Fig. 3). However, unlike PB10, R70 did not alter exchange rates at distal sites beyond α-helix B.

WECB2 strongly protected two distinct RiVax secondary structural elements: α-helix B (residues 94 to 107; peptides 32 to 36 and 38) and β-strand h (residues 110 to 122; peptides 43 to 44). WECB2's epitope, when mapped onto the solvent-accessible surface of RiVax, is considerably larger than PB10's epitope (Fig. 4). This difference may explain why WECB2 has slightly more potent toxin neutralizing activity than PB10 (34). WECB2 induced intermediate protection around α-helix C (residues 125 to 135; peptides 48 to 52), the C-terminal end of α-helix D, and the N terminus of α-helix E and the preceding loop (residues 154 to 167; peptides 65 and 67) (Fig. 4). It is interesting that within α-helix C, residues Q129 and L130 have side chains oriented toward WECB2's primary epitope (see Fig. S2 in the supplemental material), raising the possibility that the intermediate protection detected across this region is due to direct contact with WECB2 rather than to an allosteric effect. WECB2, like PB10, induced protection near RiVax's C terminus (residues 249 to 255; peptides 122, 124, and 125). In summary, the HX-MS results demonstrate that all three cluster I MAbs, PB10, R70, and WECB2, recognize epitopes focused on α-helix B, a known immunodominant element of ricin toxin (59).

Epitope mapping of the cluster II toxin-neutralizing MAbs (SyH7, PA1, PH12, and TB12). Cluster II is defined by four different MAbs: SyH7, PA1, PH12, and TB12 (Table 1). SyH7's epitope was tentatively localized by pepscan analysis to RiVax residues
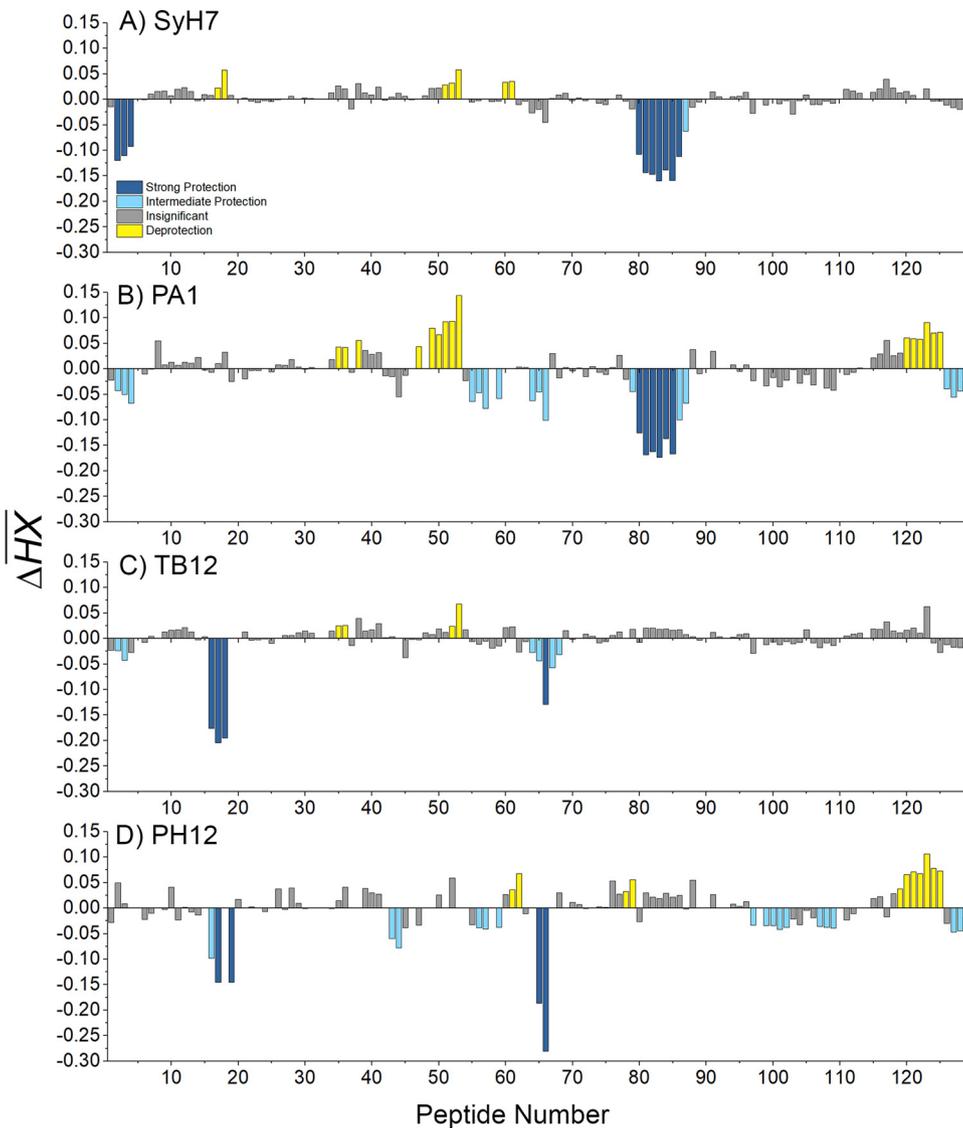
FIG 5 Relative levels of protection of RiVax peptides by SyH7, PA1, TB12, and PH12, as defined by HX-MS. The $\overline{\Delta HX}$ values for each RiVax peptide are shown for MAbs (A) SyH7, (B) PA1, (C) TB12, and (D) PH12. The $\overline{\Delta HX}$ values are color coded according to the Fig. 3 legend.

187 to 198, which correspond to α-helix F and the F-G loop (30, 34). The other three MAbs (PA1, PH12, and TB12) compete with SyH7 for binding to ricin but recognize nonlinear (discontinuous) epitopes and, therefore, were negative by pepscan analysis (34).

HX-MS analysis revealed that SyH7 strongly protected two regions of RiVax: residues 14 to 24 (peptides 2 to 4), corresponding to α-helix A and a preceding β-turn, and residues 184 to 207 (peptides 80 to 86), corresponding to α-helix F and the N-terminal half of α-helix G (Table 2 and Fig. 5 and 6). The regions of strong protection form a large patch that is situated on the "back side" of the molecule, relative to the active site. This region of RTA is proposed to initiate contact with ribosomes (15, 60). SyH7 binding also resulted in deprotection of residues 62 to 69, 129 to 135, and 148 to 151 (peptides 17 to 18, 51 to 53, and 60 to 61) (Fig. 5 and 6), which are peripheral to SyH7's core epitope. Deprotection of these peptides could be the result of relaxation of the structure through stress created by the primary antibody binding site (61).

The pattern of altered HX induced by PA1 was similar to that shown by SyH7, in that PA1 strongly protected α-helix F and the N-terminal end of α-helix G (Table 2 and
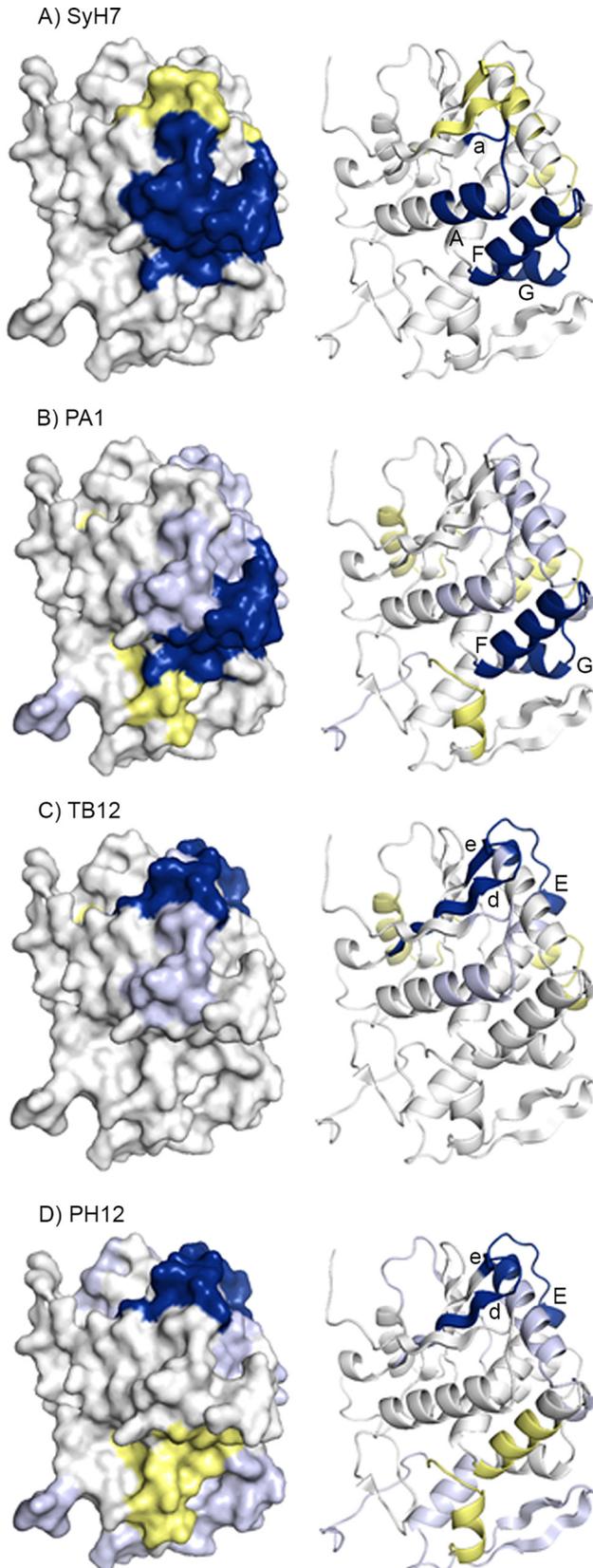
FIG 6 Visual presentation of the core epitopes of SyH7, PA1, TB12, and PH12 on RiVax. HX protection categories, as defined in the Fig. 5 legend, are shown mapped onto the structure of RiVax for (A) SyH7, (B) PA1, (C) TB12, and (D) PH12. The image is color coded according to the Fig. 5 legend. The locations of β-strands a, d, and e as well as α-helices A, E, F, and G are indicated.
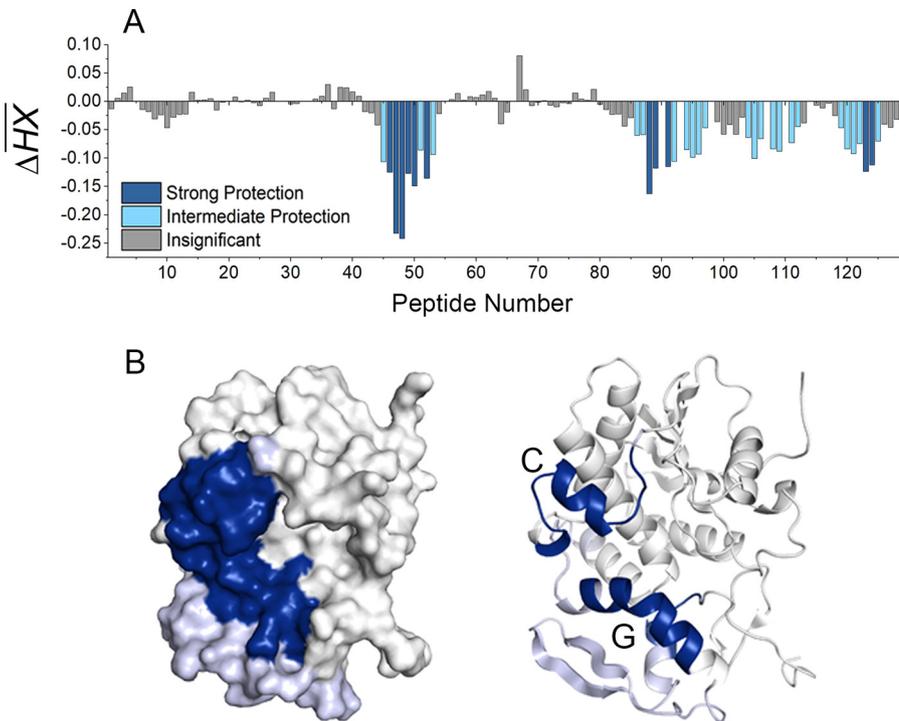
FIG 7 Localization of the core epitope of IB2 on RiVax. (A) The $\Delta\overline{HX}$ values for each RiVax peptide shown for IB2 are indicated and are color coded according to the Fig. 3 legend. (B) The HX protection categories, as defined for panel A, are shown mapped onto the structure of RiVax. The locations of α-helices C and G are indicated.

Fig. 5 and 6). PA1 differed from SyH7 in that it did not strongly protect α-helix A. Thus, PA1's core epitope appears to be nested within SyH7's epitope. If regions of intermediate protection are taken into account, however, then PA1's footprint potentially encompasses the N terminus of α-helix A (residues 14 to 24; peptides 2 to 4), α-helix D-E and the intervening loop (residues 136 to 151 and 154 to 164; peptides 55 to 57, 59, and 64 to 66), and RiVax's C terminus (residues 257 to 267; peptides 126 to 128) (Fig. 6). Without further validation studies, it would be premature to conclude that the areas of intermediate protection constitute actual antibody binding sites.

The epitopes recognized by TB12 and PH12 were also mapped with HX-MS. As shown in Fig. 5 and 6, TB12 and PH12 have very similar epitopes. Both MAbs strongly protected RiVax peptides spanning a region between β-strands d and e (residues 60 to 69; peptides 16 to 18), as well as the loop and β-turn preceding α-helix E (residues 155 to 164; peptide 66) (Table 2). The two epitopes are not identical, however, as the magnitudes of intermediate protection and zones of deprotection were different (Fig. 5 and 6). We conclude that cluster II consists of two distinct epitope subclusters: one defined by SyH7 and PA1 and the other by TB12 and PH12. These epitope mapping results partially explain the differential pairwise competition results observed by ELISA (see Fig. S1 in the supplemental material).

Epitope mapping of cluster III (IB2) and cluster IV (GD12 and JD4) MAbs. Cluster III is represented by a single MAb, IB2, whose epitope has been postulated to encompass the C terminus of RiVax (34). HX-MS analysis indicated that IB2 strongly protected RiVax's α-helix C and the following loop (peptides 46 to 50 and 52; residues 121 to 135), as well as α-helix G (residues 207 to 217; peptides 88, 89, and 91) (Fig. 7). These two strongly protected elements form a patch below and to the left of the RTA's active site (Fig. 7B). A region near the C terminus of RTA (residues 251 to 254; peptides 123 and 124) was also strongly protected by IB2.

Cluster IV is represented by two MAbs, GD12 and JD4. Based on admittedly weak reactivity with an 18-mer RTA peptide array, GD12 was proposed to recognize a linear
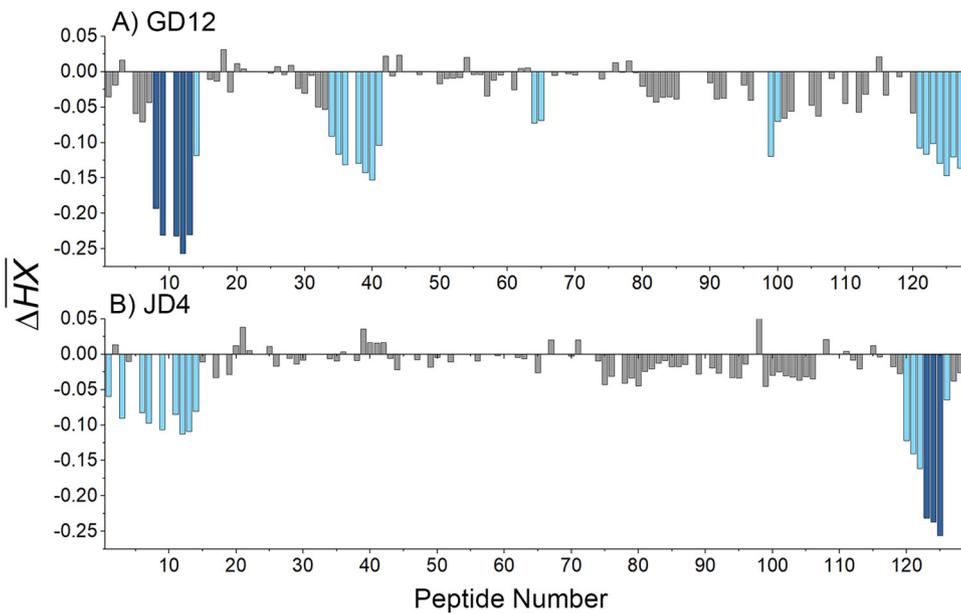
FIG 8 Relative levels of protection of RiVax peptides by GD12 and JD4, as defined by HX-MS. The $\overline{\Delta HX}$ values for each RiVax peptide are shown for MAbs (A) GD12 and (B) JD4. The $\overline{\Delta HX}$ values are color coded according to the Fig. 3 legend.

epitope encompassing residues 163 to 174 (43). However, this assignment was contradicted by the HX-MS results. Specifically, GD12 strongly protected residues 35 to 59 (peptides 8, 9, and 11 to 13), which include β-strands b and c and the two interconnecting β-turns (Fig. 8 and 9). GD12's epitope forms a "sash" from the C terminus of α-helix B to the N terminus side of β-strand d located along the back side of RTA and down to the interface with RTB. The fact that GD12's core epitope, as determined by HX-MS, is proximal to (and possibly contacts) α-helix B likely explains why the binding of GD12 to ricin is competitively inhibited by R70 and PB10 (see Fig. S1 in the supplemental material). We postulate that the reported low-affinity reactivity of GD12 with peptides spanning residues 163 to 174 may constitute a mimitope or even nonspecific binding, since most of those residues are not surface accessible on RiVax or RTA.

JD4 has relatively weak affinity for ricin toxin, possibly accounting for its lack of *in vitro* toxin-neutralizing activity (Table 1). HX-MS analysis revealed that JD4 did not strongly protect any region of RTA, except for three peptides (namely, peptides 123 to 125) corresponding to residues 249 to 255 near RTA's C terminus, which is normally a region of RTA occluded by RTB (Fig. 8 and 9). JD4 did, however, induce intermediate protection along nearly the entire length of RTA's N terminus (residues 1 to 59; Fig. 8). While the observed region of intermediate protection is consistent with the competition binding assays performed with GD12, it represents both an unusually large surface area and, most certainly, an overestimation of actual antibody contact points.

DISCUSSION

In this study, we used HX-MS to localize the epitopes on RiVax recognized by nine different previously characterized ricin toxin-neutralizing MAbs and one nonneutralizing MAb. As predicted from cross-competition binding studies, pepscan analysis, and RTA point and deletion mutant studies (30, 34, 43, 44), the nine toxin-neutralizing MAbs grouped into four spatially distinct epitope clusters, which cover approximately half the solvent-exposed surface area of the antigen (Fig. 10). By all accounts, clusters I to IV represent the most immunodominant elements on the surface of RiVax. Cluster I epitopes were centered on RiVax's α-helix B, with the epitopes recognized by PB10 and R70 being nearly identical, while WECB2, which makes additional contact with β-strand
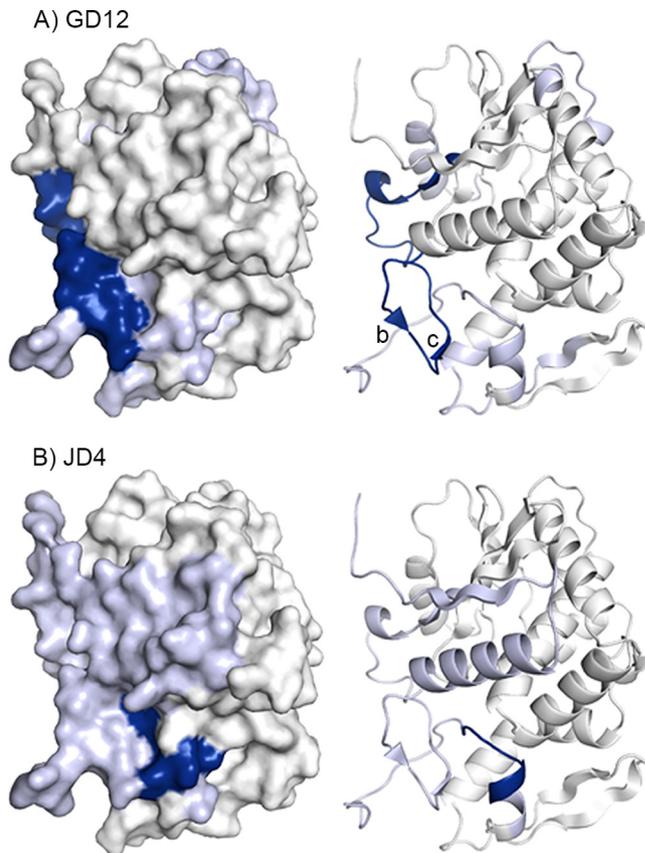
A) GD12

B) JD4

FIG 9 Visual presentation of the core epitopes of GD12 and JD4 on RiVax. Protection categories for (A) GD12 and (B) JD4, as defined in the Fig. 3 legend, are shown mapped onto RiVax. The locations of β-strands b and c are indicated.

h (residues 110 to 122), had a markedly larger footprint on RiVax. This may explain why WECB2's *in vitro* toxin-neutralizing activity was slightly more potent than that seen with PB10 and R70 (34). The cluster II epitopes were conveniently distributed into two subclusters: SyH7 and PA1 contact α-helix F and the proximal half of α-helix G, while PH12 and TB12 contact α-helices D and E (Fig. 10). IB2, the sole representative of cluster III in this study, recognizes an epitope encompassing α-helices C and G and forms a diagonal patch on RiVax that borders clusters I and II (Fig. 10). Finally, GD12, a member of cluster IV, protects β-strands b and c and N-terminal elements of d around residue 50 (Fig. 10).

The results presented here have implications for the preclinical evaluation of RiVax. It was previously reported that sera from RiVax-vaccinated rhesus macaques, as well as sera from humans, contain antibodies that compete with PB10, R70, WECB2, SyH7, and PA1 (10). We have now localized the specific epitopes on RiVax recognized by all five of those particular MAbs. As noted in a recent review (12), there is a particular need for a surrogate measure of ricin toxin vaccine potency, because neither ricin-specific serum IgG endpoint titers nor toxin-neutralizing antibody levels are sufficiently robust on their own to serve as correlates of protection. Indeed, we are currently exploring whether combinations of these MAbs may serve as tools to interrogate epitope-specific antibody responses in the serum of rodents and nonhuman primates vaccinated with RiVax and whether there is a relationship between epitope-specific responses and survival following ricin challenge (G. Van Slyke, D. Ehrbar, J. Yates, J. Westfall, and N. Mantis, unpublished data).

There are several proposed mechanisms by which RTA-specific antibodies might neutralize ricin toxin *in vitro*. Legler and colleagues recently demonstrated, using V$_H$Hs,
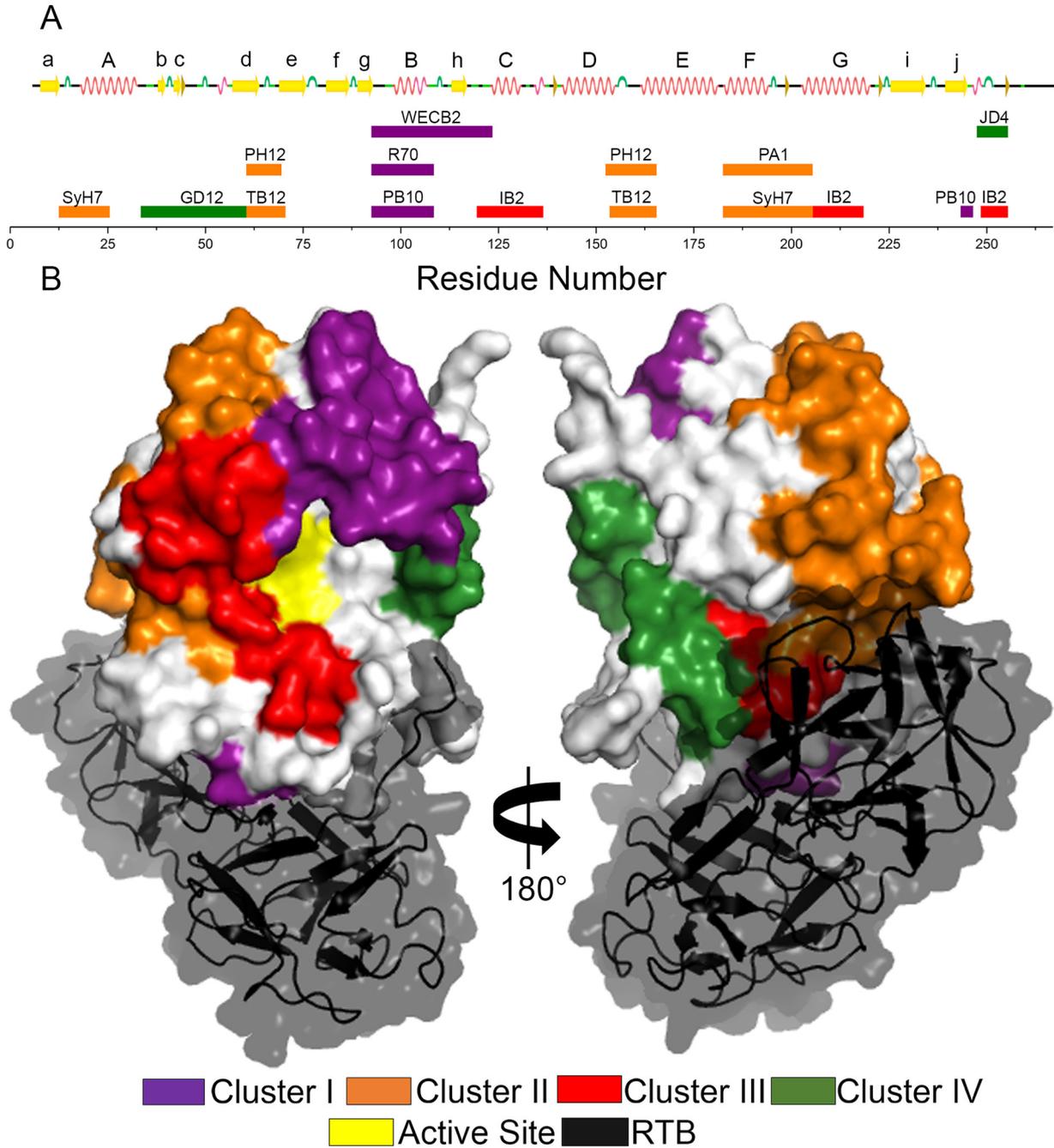
FIG 10 Summary of HX-MS epitopes on RiVax for clusters I to IV. (A) Strongly protected regions for each MAb are shown in a linear representation of the primary sequence of RiVax, aligned with a secondary structure cartoon. Coils denote helices, arrows indicate β secondary structure, and the bulges denote bends. The colored rectangles denote epitopes and are labeled with the corresponding MAb designation. The colors of the rectangles correspond to epitope clusters as denoted in panel B. (B) The strongly protected regions for each cluster are summed over all MAbs belonging to that cluster and shown mapped to the crystal structure of the ricin holotoxin (PDB ID: 2AAI) (14), with each cluster colored as indicated. Where overlaps occurred, they were resolved as follows: cluster III overwrites cluster IV; cluster II overwrites clusters III to IV; and cluster I overwrites clusters II to IV.

a correlation between an antibody's impact on RTA unfolding dynamics and *in vitro* toxin-neutralizing activity, possibly due to events associated with ricin endocytosis or retrograde transport (39). Other reports have shown that anti-RTA MAbs reduced intracellular transport of ricin from the plasma membrane to the endoplasmic reticulum (ER) and even prevented protein-disulfide isomerase (PDI)-mediated dissociation of RTA from RTB in a cell-free assay (62–64). Whether these *in vitro* activities are relevant *in vivo*

remains to be determined. The nine toxin-neutralizing MAbs characterized in this report afford passive immunity to ricin challenge in mice (30, 34), and some MAbs have even been shown to have therapeutic potential when administered several hours after toxin exposure (65, 66). A humanized version of PB10 is being evaluated in nonhuman primates as a possible therapeutic (C. Roy and L. Zeitlin, personal communication). Understanding the mechanisms by which RTA-specific antibodies protect the lung mucosa from aerosolized ricin challenge will be of particular importance, especially considering that the toxin likely engages with both alveolar macrophages and lung epithelial cells following aerosol exposure. Ricin uptake into macrophages is proposed to occur via the mannose receptor or other C-type lectins, independently of RTB-mediated retrograde transport (67, 68). Possible roles for epitope specificity in serum and mucosal ricin neutralization are under active investigation.

While this report has primarily focused on localizing neutralizing epitopes on RiVax, it should not be overlooked that a second ricin toxin subunit vaccine, RV*Ec*, was recently evaluated in humans (23). As noted above in the introduction, RV*Ec* is a truncated version of RTA that lacks domain 3 (residues 199 to 267), as well as a small hydrophobic loop in the N terminus (residues 34 to 43) (19–21). The results that have been obtained by HX-MS epitope mapping studies now explain the observation that IB2, SyH7, PA1, and GD12 fail to recognize RV*Ec*, in part or in full (34). IB2's epitope is effectively removed as a result of RV*Ec*'s C-terminal deletion (Fig. 10), while SyH7 and PA1 have greatly reduced reactivity with RV*Ec*, which can be explained by the fact that their epitopes include residues 184 to 207, while RV*Ec* terminates at residue 199. GD12 is similarly unable to recognize RV*Ec* but for a different reason. The deletion of the small loop, corresponding to residues 34 to 43, removes approximately half of GD12's epitope (residues 35 to 59). The loss of epitopes corresponding to clusters III and IV, as well as to part of cluster II, explains why RV*Ec* immunization results in a slight bias for antibodies against cluster I compared to RiVax (69). Nonetheless, in spite of lacking what are seemingly important neutralizing B cell epitopes, RV*Ec* has proven as effective as RiVax at eliciting immunity to ricin in mice across a range of doses and with different adjuvants (69, 70).

The nine toxin-neutralizing MAbs that were subjected to epitope mapping in this study (Table 1) were used in a study, reported in a companion paper, of competition ELISAs for the purpose of localizing the binding sites of a large collection of V_HHs (71). As part of that study, we reported the full-length DNA sequences, binding affinities, and neutralizing activities of 31 V_HHs against RTA, 33 against RTB, and 4 against ricin holotoxin. Remarkably, the epitopes of the RTA-specific V_HHs localized within one or more of the four clusters defined in this study (Fig. 10). The fact that no RTA-specific V_HHs that fell outside these four clusters were identified is a testament to the degree of coverage that has been achieved on the surface of RiVax with the 10 MAbs used in this study. Interestingly, the anti-RTA V_HHs fell into 11 different competition profiles, or "bins," which further resolves and refines the interrelationships among neutralizing and nonneutralizing epitopes on the surface of RTA. Roughly half of the RTA-specific V_HHs had detectable toxin-neutralizing activity, although only three were classified as showing strong activity, defined by a 50% inhibitory concentration (IC_{50}) of less than 10 nM. Localization of the binding sites of these V_HHs by competition ELISA and X-ray crystallography has revealed structural elements on RTA that likely constitute key points of toxin vulnerability (40–42). TNA was associated with V_HHs that contact (or are proposed to contact) RTA's α-helix B and/or α-helix D, defined by competition with WECB2, and was also associated with those that contact (or are proposed to contact) α-helix F and the F-G loop, defined by competition with SyH7. Another somewhat surprising finding from the companion study was the identification of a putative supercluster of epitopes situated at the RTA-RTB interface and defined by competition with SyH7. In other words, there was a population of toxin-neutralizing, RTB-specific V_HHs whose binding to ricin was inhibited by the RTA-specific MAb SyH7 and by the V_HH V5E1. Thus, the combination of competition ELISAs, HX-MS, and X-ray crystallography using murine and camelid antibodies has resulted in a high-resolution B cell

epitope map of RTA and RiVax that can now be exploited for the purpose of vaccine and therapeutic development.

MATERIALS AND METHODS

Chemicals and reagents. Sodium chloride (crystalline; certified by the American Chemical Society [ACS]), deuterium oxide, and guanidine hydrochloride were purchased from Fisher Scientific (Fair Lawn, NJ). All other chemicals were obtained from Sigma-Aldrich, Inc. (St. Louis, MO), unless noted otherwise. RiVax was expressed and purified as described previously (72), divided into aliquots, and stored at −80°C. After they were thawed, RiVax samples were buffer exchanged into 10 mM sodium phosphate–150 mM sodium chloride (pH 7.4). RiVax samples were over 98% pure as measured by sedimentation velocity-analytical ultracentrifugation (SV-AUC) (data not shown). Proteolytic cleavage performed with an N-terminal 6×His affinity tag resulted in a nonnative N-terminal alanine in the amino acid sequence. This alanine is assigned as residue zero in order to align the sequence numbering with the native RTA sequence.

RTA-specific MAbs. The MAbs used in this study are shown in Table 1 and were purified by protein A chromatography at the Dana Farber Cancer Institute (DFCI) Monoclonal Antibody Core Facility (Boston, MA). Immunocompetition sandwich ELISAs (shown in Fig. S1 in the supplemental material) were done as follows. Nunc Immuno MicroWell 96-well plates were coated overnight with capture anti-RTA MAbs (1 μg/ml). The following day, the plates were blocked with 2% goat serum, washed, and then overlaid with a mixture of biotin-tagged ricin and competitor MAb (10 μg/ml). The amount of biotin-ricin used in the competition ELISA was adjusted to the 90% effective concentration (EC$_{90}$) for each capture MAb. After 1 h of incubation, the plates were washed and developed with streptavidin-horseradish peroxidase (HRP) antibody (Southern Biotech) (1:500) and TMB (3,3′,5,5′-tetramethylbenzidine). The percentage of inhibition of ricin binding to the capture MAb in the present of a competitor MAb was calculated from the values corresponding to the optical density at 450 nm (OD$_{450}$) as follows: 1 − OD$_{450}$ value (biotin-ricin plus competitor MAb)/OD$_{450}$ value (biotin-ricin without competitor MAb) × 100.

HX-MS. HX-MS experiments were conducted using a LEAP H/DX PAL system (Carrboro, NC) and a model 6530 quadrupole time of flight (QTOF) mass spectrometer (Agilent, Santa Clara, CA). Three microliters of RiVax prepared at 20 μM was incubated with 27 μl of deuterated buffer (10 mM sodium phosphate, 150 mM sodium chloride, pD 7.4) at 25°C for 13 to 86,400 s. The final concentration of the MAbs was 40 μM and that of RiVax was 20 μM, resulting in a 2-fold molar excess of antibody. Incubation at each HX time was performed in triplicate. For experiments performed in the presence of MAb, RiVax was prepared at 20 μM with a MAb concentration of 40 μM. Hydrogen exchange was quenched using 200 mM phosphate–4 M guanidinium chloride (pH 2.5). Fifty-five microliters of the quenched sample was then injected into a liquid chromatography (LC) system from online proteolysis performed using an immobilized pepsin column (73) followed by desalting and chromatographic separation. The LC method used included the use of an 18-min segmented gradient from 1% to 95% mobile phase B, with mobile phase A consisting of 0.1% formic acid and mobile phase B of 90% acetonitrile–0.1% formic acid. Tandem MS (MS/MS) analysis was used to generate a peptide map of RiVax providing 100% sequence coverage with 129 peptides (Toth et al., unpublished). The HX data were processed using HDExaminer software (Sierra Analytics, Modesto, CA). Data were corrected for maximum deuteration as measured with a deuteration control (RiVax was labeled in a pD 8 buffer for 18 h and then digested and analyzed as described above). Backbone flexibility was quantified using the fraction of exchange after the shortest HX time (13 s) as follows:

$$\text{flexibility}\ (\%) = \frac{\Delta m}{\Delta m_\infty} \times 100\%$$

where Δm denotes measured mass increase (HX) and the infinity subscript designates the measured HX for the deuteration control. For epitope mapping, HX data for each peptide from all HX times were averaged into a single differential value representing free RTA minus MAb-bound RTA (ΔHX). A combination of significance testing and k-means clustering was applied and will be described elsewhere (Toth et al., unpublished). In this work, epitopes were defined using only the most strongly protected category from the k-means clustering.

Molecular graphics. All structures were displayed using PyMOL Molecular Graphics System Version 1.8 (PyMOL Molecular Graphics System; Schrodinger LLC, San Diego, CA), ricin holotoxin (PDB identifier [ID]: 2AAI) (14), RTA (PDB ID: 1RTC) (74), or RiVax (PDB ID: 3SRP) (18). In mapping HX data to the structures, residue conflicts from overlapping peptides were resolved as follows: intermediate protection overwrote insignificant protection, and strong protection overwrote intermediate protection. In addition, since the first two residues typically undergo rapid back-exchange during analysis (75), the first two residues in each peptide were ignored during epitope mapping.

SUPPLEMENTAL MATERIAL

Supplemental material for this article may be found at https://doi.org/10.1128/CVI .00237-17.

SUPPLEMENTAL FILE 1, PDF file, 0.3 MB.

ACKNOWLEDGMENTS

REFERENCES

1. Griffiths GD. 2011. Understanding ricin from a defensive viewpoint. Toxins (Basel) 3:1373–1392. https://doi.org/10.3390/toxins3111373.
2. Reisler RB, Smith LA. 2012. The need for continued development of ricin countermeasures. Adv Prev Med 2012:149737. https://doi.org/10.1155/2012/149737.
3. Bradberry SM, Dickers KJ, Rice P, Griffiths GD, Vale JA. 2003. Ricin poisoning. Toxicol Rev 22:65–70. https://doi.org/10.2165/00139709-200322010-00007.
4. Simmons BM, Russell JH. 1985. A single affinity column step method for the purification of ricin toxin from castor beans (Ricinus communis). Anal Biochem 146:206–210. https://doi.org/10.1016/0003-2697(85)90417-8.
5. Tesh VL. 2012. The induction of apoptosis by Shiga toxins and ricin. Curr Top Microbiol Immunol 357:137–178.
6. Endo Y, Mitsui K, Motizuki M, Tsurugi K. 1987. The mechanism of action of ricin and related toxic lectins on eukaryotic ribosomes. The site and the characteristics of the modification in 28 S ribosomal RNA caused by the toxins. J Biol Chem 262:5908–5912.
7. Endo Y, Tsurugi K. 1987. RNA N-glycosidase activity of ricin A-chain. Mechanism of action of the toxic lectin ricin on eukaryotic ribosomes. J Biol Chem 262:8128–8130.
8. Pincus SH, Bhaskaran M, Brey RN, III, Didier PJ, Doyle-Meyers LA, Roy CJ. 2015. Clinical and pathological findings associated with aerosol exposure of macaques to ricin toxin. Toxins (Basel) 7:2121–2133. https://doi.org/10.3390/toxins7062121.
9. Smallshaw JE, Richardson JA, Vitetta ES. 2007. RiVax, a recombinant ricin subunit vaccine, protects mice against ricin delivered by gavage or aerosol. Vaccine 25:7459–7469. https://doi.org/10.1016/j.vaccine.2007.08.018.
10. Roy CJ, Brey RN, Mantis NJ, Mapes K, Pop IV, Pop LM, Ruback S, Killeen SZ, Doyle-Meyers L, Vinet-Oliphant HS, Didier PJ, Vitetta ES. 2015. Thermostable ricin vaccine protects rhesus macaques against aerosolized ricin: epitope-specific neutralizing antibodies correlate with protection. Proc Natl Acad Sci U S A 112:3782–3787. https://doi.org/10.1073/pnas.1502585112.
11. Audi J, Belson M, Patel M, Schier J, Osterloh J. 2005. Ricin poisoning: a comprehensive review. JAMA 294:2342–2351. https://doi.org/10.1001/jama.294.18.2342.
12. Vance DJ, Mantis NJ. 2016. Progress and challenges associated with the development of ricin toxin subunit vaccines. Expert Rev Vaccines 15:1213–1222. https://doi.org/10.1586/14760584.2016.1168701.
13. Montfort W, Villafranca JE, Monzingo AF, Ernst SR, Katzin B, Rutenber E, Xuong NH, Hamlin R, Robertus JD. 1987. The three-dimensional structure of ricin at 2.8 A. J Biol Chem 262:5398–5403.
14. Rutenber E, Katzin BJ, Ernst S, Collins EJ, Mlsna D, Ready MP, Robertus JD. 1991. Crystallographic refinement of ricin to 2.5 A. Proteins 10:240–250. https://doi.org/10.1002/prot.340100308.
15. Katzin BJ, Collins EJ, Robertus JD. 1991. Structure of ricin A-chain at 2.5 A. Proteins 10:251–259. https://doi.org/10.1002/prot.340100309.
16. Smallshaw JE, Firan A, Fulmer JR, Ruback SL, Ghetie V, Vitetta ES. 2002. A novel recombinant vaccine which protects mice against ricin intoxication. Vaccine 20:3422–3427. https://doi.org/10.1016/S0264-410X(02)00312-2.
17. Smallshaw JE, Ghetie V, Rizo J, Fulmer JR, Trahan LL, Ghetie MA, Vitetta ES. 2003. Genetic engineering of an immunotoxin to eliminate pulmonary vascular leak in mice. Nat Biotechnol 21:387–391. https://doi.org/10.1038/nbt800.
18. Legler PM, Brey RN, Smallshaw JE, Vitetta ES, Millard CB. 2011. Structure of RiVax: a recombinant ricin vaccine. Acta Crystallogr D Biol Crystallogr 67:826–830. https://doi.org/10.1107/S0907444911026771.
19. Carra JH, Wannemacher RW, Tammariello RF, Lindsey CY, Dinterman RE, Schokman RD, Smith LA. 2007. Improved formulation of a recombinant ricin A-chain vaccine increases its stability and effective antigenicity. Vaccine 25:4149–4158. https://doi.org/10.1016/j.vaccine.2007.03.011.
20. McHugh CA, Tammariello RF, Millard CB. 2004. Improved stability of a protein vaccine through elimination of a partially unfolded state. Protein Sci 13:2736–2743. https://doi.org/10.1110/ps.04897904.
21. Olson MA, Carra JH, Roxas-Duncan V, Wannemacher RW, Smith LA, Millard CB. 2004. Finding a new vaccine in the ricin protein fold. Protein Eng Des Sel 17:391–397. https://doi.org/10.1093/protein/gzh043.
22. Williamson ED, Duchars MG, Kohberger R. 2010. Predictive models and correlates of protection for testing biodefence vaccines. Expert Rev Vaccines 9:527–537. https://doi.org/10.1586/erv.10.22.
23. Pittman PR, Reisler RB, Lindsey CY, Guerena F, Rivard R, Clizbe DP, Chambers M, Norris S, Smith LA. 2015. Safety and immunogenicity of ricin vaccine, RVEc, in a phase 1 clinical trial. Vaccine 33:7299–7306. https://doi.org/10.1016/j.vaccine.2015.10.094.
24. Vitetta ES, Smallshaw JE, Coleman E, Jafri H, Foster C, Munford R, Schindler J. 2006. A pilot clinical trial of a recombinant ricin vaccine in normal humans. Proc Natl Acad Sci U S A 103:2268–2273. https://doi.org/10.1073/pnas.0510893103.
25. Vitetta ES, Smallshaw JE, Schindler J. 2012. Pilot phase IB clinical trial of an alhydrogel-adsorbed recombinant ricin vaccine. Clin Vaccine Immunol 19:1697–1699. https://doi.org/10.1128/CVI.00381-12.
26. Colombatti M, Johnson VG, Skopicki HA, Fendley B, Lewis MS, Youle RJ. 1987. Identification and characterization of a monoclonal antibody recognizing a galactose-binding domain of the toxin ricin. J Immunol 138:3339–3344.
27. Colombatti M, Pezzini A, Colombatti A. 1986. Monoclonal antibodies against ricin: effects on toxin function. Hybridoma 5:9–19. https://doi.org/10.1089/hyb.1986.5.9.
28. Maddaloni M, Cooke C, Wilkinson R, Stout AV, Eng L, Pincus SH. 2004. Immunological characteristics associated with the protective efficacy of antibodies to ricin. J Immunol 172:6221–6228. https://doi.org/10.4049/jimmunol.172.10.6221.
29. Noy-Porat T, Rosenfeld R, Ariel N, Epstein E, Alcalay R, Zvi A, Kronman C, Ordentlich A, Mazor O. 3 March 2016. Isolation of anti-ricin protective antibodies exhibiting high affinity from immunized non-human primates. Toxins (Basel) https://doi.org/10.3390/toxins8030064.
30. O'Hara JM, Neal LM, McCarthy EA, Kasten-Jolly JA, Brey RN, III, Mantis NJ. 2010. Folding domains within the ricin toxin A subunit as targets of protective antibodies. Vaccine 28:7035–7046. https://doi.org/10.1016/j.vaccine.2010.08.020.
31. O'Hara JM, Whaley K, Pauly M, Zeitlin L, Mantis NJ. 2012. Plant-based expression of a partially humanized neutralizing monoclonal IgG directed against an immunodominant epitope on the ricin toxin A subunit. Vaccine 30:1239–1243. https://doi.org/10.1016/j.vaccine.2011.12.058.
32. O'Hara JM, Yermakova A, Mantis NJ. 2012. Immunity to ricin: fundamental insights into toxin-antibody interactions. Curr Top Microbiol Immunol 357:209–241. https://doi.org/10.1007/82_2011_193.
33. Rong Y, Van Slyke G, Vance DJ, Westfall J, Ehrbar D, Mantis NJ. 2017. Spatial location of neutralizing and non-neutralizing B cell epitopes on domain 1 of ricin toxin's binding subunit. PLoS One 12:e0180999. https://doi.org/10.1371/journal.pone.0180999.
34. O'Hara JM, Kasten-Jolly JC, Reynolds CE, Mantis NJ. 2014. Localization of non-linear neutralizing B cell epitopes on ricin toxin's enzymatic subunit (RTA). Immunol Lett 158:7–13. https://doi.org/10.1016/j.imlet.2013.11.009.

35. Rosenfeld R, Alcalay R, Mechaly A, Lapidoth G, Epstein E, Kronman C, Fleishman SJ, Mazor O. 2017. Improved antibody-based ricin neutralization by affinity maturation is correlated with slower off-rate values. Protein Eng Des Sel 30:611–617. https://doi.org/10.1093/protein/gzx028.

36. Castelletti D, Fracasso G, Righetti S, Tridente G, Schnell R, Engert A, Colombatti M. 2004. A dominant linear B-cell epitope of ricin A-chain is the target of a neutralizing antibody response in Hodgkin's lymphoma patients treated with an anti-CD25 immunotoxin. Clin Exp Immunol 136:365–372. https://doi.org/10.1111/j.1365-2249.2004.02442.x.

37. Dai J, Zhao L, Yang H, Guo H, Fan K, Wang H, Qian W, Zhang D, Li B, Wang H, Guo Y. 2011. Identification of a novel functional domain of ricin responsible for its potent toxicity. J Biol Chem 286:12166–12171. https://doi.org/10.1074/jbc.M110.196584.

38. Lemley PV, Amanatides P, Wright DC. 1994. Identification and characterization of a monoclonal antibody that neutralizes ricin toxicity in vitro and in vivo. Hybridoma 13:417–421. https://doi.org/10.1089/hyb.1994.13.417.

39. Legler PM, Compton JR, Hale ML, Anderson GP, Olson MA, Millard CB, Goldman ER. 2017. Stability of isolated antibody-antigen complexes as a predictive tool for selecting toxin neutralizing antibodies. MAbs 9:43–57. https://doi.org/10.1080/19420862.2016.1236882.

40. Rudolph MJ, Vance DJ, Cassidy MS, Rong Y, Mantis NJ. 2017. Structural analysis of single domain antibodies bound to a second neutralizing hot spot on ricin toxin's enzymatic subunit. J Biol Chem 292:872–883. https://doi.org/10.1074/jbc.M116.758102.

41. Rudolph MJ, Vance DJ, Cassidy MS, Rong Y, Shoemaker CB, Mantis NJ. 2016. Structural analysis of nested neutralizing and non-neutralizing B cell epitopes on ricin toxin's enzymatic subunit. Proteins 84:1162–1172. https://doi.org/10.1002/prot.25062.

42. Rudolph MJ, Vance DJ, Cheung J, Franklin MC, Burshteyn F, Cassidy MS, Gary EN, Herrera C, Shoemaker CB, Mantis NJ. 26 August 2014. Crystal structures of ricin toxin's enzymatic subunit (RTA) in complex with neutralizing and non-neutralizing single-chain antibodies. J Mol Biol https://doi.org/10.1016/j.jmb.2014.05.026.

43. Neal LM, O'Hara J, Brey RN, III, Mantis NJ. 2010. A monoclonal immunoglobulin G antibody directed against an immunodominant linear epitope on the ricin A chain confers systemic and mucosal immunity to ricin. Infect Immun 78:552–561. https://doi.org/10.1128/IAI.00796-09.

44. Vance DJ, Mantis NJ. 2012. Resolution of two overlapping neutralizing B cell epitopes within a solvent exposed, immunodominant alpha-helix in ricin toxin's enzymatic subunit. Toxicon 60:874–877. https://doi.org/10.1016/j.toxicon.2012.06.014.

45. Brown KA, Wilson DJ. 7 August 2017. Bottom-up hydrogen deuterium exchange mass spectrometry: data analysis and interpretation. Analyst https://doi.org/10.1039/c7an00662d.

46. Chen E, Salinas ND, Huang Y, Ntumngia F, Plasencia MD, Gross ML, Adams JH, Tolia NH. 2016. Broadly neutralizing epitopes in the Plasmodium vivax vaccine candidate Duffy Binding Protein. Proc Natl Acad Sci U S A 113:6277–6282. https://doi.org/10.1073/pnas.1600488113.

47. Gribenko AV, Parris K, Mosyak L, Li S, Handke L, Hawkins JC, Severina E, Matsuka YV, Anderson AS. 2016. High resolution mapping of bactericidal monoclonal antibody binding epitopes on Staphylococcus aureus antigen MntC. PLoS Pathog 12:e1005908. https://doi.org/10.1371/journal.ppat.1005908.

48. Liang Y, Guttman M, Davenport TM, Hu SL, Lee KK. 2016. Probing the impact of local structural dynamics of conformational epitopes on antibody recognition. Biochemistry 55:2197–2213. https://doi.org/10.1021/acs.biochem.5b01354.

49. Lim XX, Chandramohan A, Lim XE, Crowe JE, Jr, Lok SM, Anand GS. 2017. Epitope and paratope mapping reveals temperature-dependent alterations in the dengue-antibody interface. Structure 25:1391–1402.e3. https://doi.org/10.1016/j.str.2017.07.007.

50. Malito E, Faleri A, Lo Surdo P, Veggi D, Maruggi G, Grassi E, Cartocci E, Bertoldi I, Genovese A, Santini L, Romagnoli G, Borgogni E, Brier S, Lo Passo C, Domina M, Castellino F, Felici F, van der Veen S, Johnson S, Lea SM, Tang CM, Pizza M, Savino S, Norais N, Rappuoli R, Bottomley MJ, Masignani V. 2013. Defining a protective epitope on factor H binding protein, a key meningococcal virulence factor and vaccine antigen. Proc Natl Acad Sci U S A 110:3304–3309. https://doi.org/10.1073/pnas.1222845110.

51. Bazzoli A, Vance DJ, Rudolph MJ, Rong Y, Angalakurthi SK, Toth RT, IV, Middaugh CR, Volkin DB, Weis DD, Karanicolas J, Mantis NJ. 4 August 2017. Using homology modeling to interrogate binding affinity in neutralization of ricin toxin by a family of single domain antibodies. Proteins https://doi.org/10.1002/prot.25353.

52. Davenport TM, Gorman J, Joyce MG, Zhou T, Soto C, Guttman M, Moquin S, Yang Y, Zhang B, Doria-Rose NA, Hu SL, Mascola JR, Kwong PD, Lee KK. 2016. Somatic hypermutation-induced changes in the structure and dynamics of HIV-1 broadly neutralizing antibodies. Structure 24:1346–1357. https://doi.org/10.1016/j.str.2016.06.012.

53. Hnida K, Stamnaes J, du Pre MF, Mysling S, Jorgensen TJ, Sollid LM, Iversen R. 2016. Epitope-dependent functional effects of celiac disease autoantibodies on transglutaminase 2. J Biol Chem 291:25542–25552. https://doi.org/10.1074/jbc.M116.738161.

54. Abbott WM, Damschroder MM, Lowe DC. 2014. Current approaches to fine mapping of antigen-antibody interactions. Immunology 142:526–535. https://doi.org/10.1111/imm.12284.

55. Chalmers MJ, Busby SA, Pascal BD, West GM, Griffin PR. 2011. Differential hydrogen/deuterium exchange mass spectrometry analysis of protein-ligand interactions. Expert Rev Proteomics 8:43–59. https://doi.org/10.1586/epr.10.109.

56. Hvidt A, Wallevik K. 1972. Conformational changes in human serum albumin as revealed by hydrogen-deuterium exchange studies. J Biol Chem 247:1530–1535.

57. Li J, Wei H, Krystek SR, Jr, Bond D, Brender TM, Cohen D, Feiner J, Hamacher N, Harshman J, Huang RY, Julien SH, Lin Z, Moore K, Mueller L, Noriega C, Sejwal P, Sheppard P, Stevens B, Chen G, Tymiak AA, Gross ML, Schneeweis LA. 2017. Mapping the energetic epitope of an antibody/interleukin-23 interaction with hydrogen/deuterium exchange, fast photochemical oxidation of proteins mass spectrometry, and alanine shave mutagenesis. Anal Chem 89:2250–2258. https://doi.org/10.1021/acs.analchem.6b03058.

58. Mazur SJ, Weber DP. 2017. The area between exchange curves as a measure of conformational differences in hydrogen-deuterium exchange mass spectrometry studies. J Am Soc Mass Spectrom 28:978–981. https://doi.org/10.1007/s13361-017-1615-1.

59. Lebeda FJ, Olson MA. 1999. Prediction of a conserved, neutralizing epitope in ribosome-inactivating proteins. Int J Biol Macromol 24:19–26. https://doi.org/10.1016/S0141-8130(98)00059-2.

60. Li XP, Chiou JC, Remacha M, Ballesta JP, Tumer NE. 2009. A two-step binding model proposed for the electrostatic interactions of ricin a chain with ribosomes. Biochemistry 48:3853–3863. https://doi.org/10.1021/bi802371h.

61. Buchenberg S, Sittel F, Stock G. 31 July 2017. Time-resolved observation of protein allosteric communication. Proc Natl Acad Sci U S A https://doi.org/10.1073/pnas.1707694114.

62. Song K, Mize RR, Marrero L, Corti M, Kirk JM, Pincus SH. 2013. Antibody to ricin a chain hinders intracellular routing of toxin and protects cells even after toxin has been internalized. PLoS One 8:e62417. https://doi.org/10.1371/journal.pone.0062417.

63. O'Hara JM, Mantis NJ. 2013. Neutralizing monoclonal antibodies against ricin's enzymatic subunit interfere with protein disulfide isomerase-mediated reduction of ricin holotoxin in vitro. J Immunol Methods 395:71–78. https://doi.org/10.1016/j.jim.2013.06.004.

64. Yermakova A, Klokk TI, O'Hara JM, Cole R, Sandvig K, Mantis NJ. 2016. Neutralizing monoclonal antibodies against disparate epitopes on ricin toxin's enzymatic subunit interfere with intracellular toxin transport. Sci Rep 6:22721. https://doi.org/10.1038/srep22721.

65. Sully EK, Whaley KJ, Bohorova N, Bohorov O, Goodman C, Kim do H, Pauly MH, Velasco J, Hiatt E, Morton J, Swope K, Roy CJ, Zeitlin L, Mantis NJ. 2014. Chimeric plantibody passively protects mice against aerosolized ricin challenge. Clin Vaccine Immunol 21:777–782. https://doi.org/10.1128/CVI.00003-14.

66. Van Slyke G, Sully EK, Bohorova N, Bohorov O, Kim D, Pauly MH, Whaley KJ, Zeitlin L, Mantis NJ. 2016. Humanized monoclonal antibody that passively protects mice against systemic and intranasal ricin toxin challenge. Clin Vaccine Immunol 23:795–799. https://doi.org/10.1128/CVI.00088-16.

67. Gage E, Hernandez MO, O'Hara JM, McCarthy EA, Mantis NJ. 2011. Role of the mannose receptor (CD206) in immunity to ricin toxin. Toxins (Basel) 3:1131–1145. https://doi.org/10.3390/toxins3091131.

68. Simmons BM, Stahl PD, Russell JH. 1986. Mannose receptor-mediated uptake of ricin toxin and ricin A chain by macrophages. Multiple intracellular pathways for a chain translocation. J Biol Chem 261:7912–7920.

69. O'Hara JM, Brey RN, III, Mantis NJ. 2013. Comparative efficacy of two leading candidate ricin toxin a subunit vaccines in mice. Clin Vaccine Immunol 20:789–794. https://doi.org/10.1128/CVI.00098-13.

70. Vance DJ, Greene CJ, Rong Y, Mandell LM, Connell TD, Mantis NJ. 2015. Comparative adjuvant effects of type II heat-labile enterotoxins in combination with two different candidate ricin toxin vaccine antigens. Clin Vaccine Immunol 22:1285–1293. https://doi.org/10.1128/CVI.00402-15.

71. Vance DJ, Tremblay JM, Rong Y, Angalakurthi SK, Volkin DB, Middaugh CR, Weis DD, Shoemaker CB, Mantis NJ. 2017. High-resolution epitope positioning of a large collection of neutralizing and nonneutralizing single-domain antibodies on the enzymatic and binding subunits of ricin toxin. Clin Vaccine Immunol 24:e00236-17. https://doi.org/10.1128/CVI.00236-17.

72. Wahome N, Sully E, Singer C, Thomas JC, Hu L, Joshi SB, Volkin DB, Fang J, Karanicolas J, Jacobs DJ, Mantis NJ, Middaugh CR. 2016. Novel ricin subunit antigens with enhanced capacity to elicit toxin-neutralizing antibody responses in mice. J Pharm Sci 105:1603–1613. https://doi.org/10.1016/j.xphs.2016.02.009.

73. Busby SA, Chalmers MJ, Griffin PR. 2007. Improving digestion efficiency under H/D exchange conditions with activated pepsinogen coupled columns. Int J Mass Spectrom 259:130–139. https://doi.org/10.1016/j.ijms.2006.08.006.

74. Mlsna D, Monzingo AF, Katzin BJ, Ernst S, Robertus JD. 1993. Structure of recombinant ricin A chain at 2.3 A. Protein Sci 2:429–435. https://doi.org/10.1002/pro.5560020315.

75. Bai Y, Milne JS, Mayne L, Englander SW. 1993. Primary structure effects on peptide group hydrogen exchange. Proteins 17:75–86. https://doi.org/10.1002/prot.340170110.